HHS Public Access

Author manuscript

*Clin Cancer Res*. Author manuscript; available in PMC 2019 December 01.

Published in final edited form as:

*Clin Cancer Res*. 2018 December 01; 24(23): 5883–5894. doi:10.1158/1078-0432.CCR-17-3668.

# A visually apparent and quantifiable CT imaging feature identifies biophysical subtypes of pancreatic ductal adenocarcinoma

**Eugene J Koay**[#1,*], **Yeonju Lee**[#1], **Vittorio Cristini**[2,15,17], **John S. Lowengrub**[3,3a,3b,3c], **Ya'an Kang**[4], **F. Anthony San Lucas**[5], **Brian P. Hobbs**[6], **Rong Ye**[6], **Dalia Elganainy**[1], **Muayad Almahariq**[7], **Ahmed M. Amer**[1], **Deyali Chatterjee**[8], **Huaming Yan**[3], **Peter C. Park**[9], **Mayrim V. Rios Perez**[4], **Dali Li**[5], **Naveen Garg**[10], **Kim A. Reiss**[11], **Shun Yu**[12], **Anil Chauhan**[13], **Mohamed Zaid**[1], **Newsha Nikzad**[1], **Robert A. Wolff**[14], **Milind Javle**[14], **Gauri R. Varadhachary**[14], **Rachna T. Shroff**[14], **Prajnan Das**[1], **Jeffrey E. Lee**[4], **Mauro Ferrari**[15], **Anirban Maitra**[5,8], **Cullen M. Taniguchi**[1], **Michael P. Kim**[4], **Christopher H. Crane**[16], **Matthew H. Katz**[4], **Huamin Wang**[8], **Priya Bhosale**[10], **Eric P. Tamm**[10], and **Jason B. Fleming**[4]

[1]Department of Radiation Oncology, The University of Texas MD Anderson Cancer Center, Houston, Texas.

[2]Center for Precision Biomedicine, The University of Texas Health Science Center, Houston, Texas.

[3]Department of Mathematics, University of California, Irvine, California.

[3a]Department of Biomedical Engineering, University of California, Irvine, California.

[3b]Chao Family Comprehensive Cancer Center, University of California, Irvine, California.

[3c]Center for Complex Biological Systems, University of California, Irvine, California.

[4]Department of Surgical Oncology, The University of Texas MD Anderson Cancer Center, Houston, Texas.

[5]Sheikh Ahmed Center for Pancreatic Cancer Research, The University of Texas MD Anderson Cancer Center, Houston, Texas.

[6]Department of Biostatistics, The University of Texas MD Anderson Cancer Center, Houston, Texas.

[*]Corresponding author: Eugene J. Koay, M.D., Ph.D., Department of Radiation Oncology, Unit 97, The University of Texas MD Anderson Cancer Center, Houston, TX 77584. ekoay@mdanderson.org.

Author contributions:

Study concept and design: E. Koay, Y. Lee, V. Cristini, J. B. Fleming

Acquisition of data: E. Koay, Y. Lee, Y. Kang, A. S. Lucas, C. M. Taniguchi, M. Almahariq, A. Amer, D. Chatterjee, J. Lowengrub, H. Yan, P. C. Park, M. Zaid, N. Nikzad, M. V. R. Perez, D. Li, N. Garg, A. Maitra, C. H. Crane, M. H. Katz, H. Wang, P. Bhosale, E. Tamm, J. B. Fleming

Analysis and interpretation of data: All authors

Drafting of the manuscript: E. Koay, Y. Lee, V. Cristini, J. B. Fleming

Critical revision of the manuscript for important intellectual content: All authors

Statistical analysis: B. P. Hobbs, R. Ye, E. Koay, Y. Lee

Obtained funding: E. Koay, V. Cristini, J. Lowengrub, M. Ferrari, A. Maitra, J. B. Fleming

**Conflict of interest disclosure statement:** The authors declare no potential conflicts of interest.

[7]Deparment of Pharmacology and Toxicology, University of Texas Medical Branch, Galveston, Texas.

[8]Department of Pathology, The University of Texas MD Anderson Cancer Center, Houston, Texas.

[9]Department of Radiation Physics, The University of Texas MD Anderson Cancer Center, Houston, Texas.

[10]Department of Diagnostic Radiology, The University of Texas MD Anderson Cancer Center, Houston, Texas.

[11]Department of Medical Oncology, The University of Pennsylvania Abramson Cancer Center, Philadelphia, Pennsylvania

[12]Department of Internal Medicine, The University of Pennsylvania, Philadelphia, Pennsylvania

[13]Department of Radiology, The University of Pennsylvania, Philadelphia, Pennsylvania

[14]Department of Gastrointestinal Medical Oncology, The University of Texas MD Anderson Cancer Center, Houston, Texas.

[15]Department of Nanomedicine, Houston Methodist Research Institute, Houston, Texas.

[16]Department of Radiation Oncology, Memorial Sloan Cancer Center, New York, New York

[17]Department of Imaging Physics, The University of Texas MD Anderson Cancer Center, Houston, Texas.

[#] These authors contributed equally to this work.

## Abstract

**Background and aims:** Pancreatic ductal adenocarcinoma (PDAC) is a heterogeneous disease with variable presentations and natural histories of disease. We hypothesized that different morphologic characteristics of PDAC tumors on diagnostic computed tomography (CT) scans would reflect their underlying biology.

**Methods:** We developed a quantitative method to categorize the PDAC morphology on pre-therapy CT scans from multiple datasets of patients with resectable and metastatic disease, and correlated these patterns with clinical/pathologic measurements. We modeled macroscopic lesion growth computationally to test the effects of stroma on morphological patterns, hypothesizing that the balance of proliferation and local migration rates of the cancer cells would determine tumor morphology.

**Results:** In localized and metastatic PDAC, quantifying the change in enhancement on CT scans at the interface between tumor and parenchyma (delta) demonstrated that patients with conspicuous (high delta) tumors had significantly less stroma, higher likelihood of multiple common pathway mutations, more mesenchymal features, higher likelihood of early distant metastasis, and shorter survival times compared with those with inconspicuous (low delta) tumors. Pathological measurements of stromal and mesenchymal features of the tumors supported the mathematical model's underlying theory for PDAC growth.

**Conclusion:** At baseline diagnosis, a visually striking and quantifiable CT imaging feature reflects the molecular and pathological heterogeneity of PDAC, and may be used to stratify

patients into distinct subtypes. Moreover, growth patterns of PDAC may be described using physical principles, enabling new insights into diagnosis and treatment of this deadly disease.

### Keywords

Pancreatic cancer; Subtypes; Biomarker; Imaging; Stroma

## INTRODUCTION

Pancreatic ductal adenocarcinoma (PDAC) is associated with early distant metastasis (DM) and resistance to chemotherapy and radiation. However, this disease has substantial heterogeneity in biophysical features and in outcomes for patients (1–5). The identification of a biomarker that distinguishes patients with more aggressive disease from those with less aggressive disease would enable more rational therapeutic choices.

One such biomarker in PDAC may involve the stroma, elements of which have been linked with suppression of metastatic spread of the cancer cells (6–8). Notably, the stroma changes in response to therapy, and the nature of those changes may be associated with more aggressive cancer biology (9). The native and dynamic roles of the stroma remain areas of intense scientific investigation. Clarifying the role of stroma is thought to have important clinical implications that could affect patient survival.

We previously showed that the stroma may represent a physical barrier to drug delivery in PDAC (3). We further demonstrated that mass transport properties derived from CT scans correlated with the delivery of, response to, and outcome after gemcitabine-based therapies (2,3). These findings suggested that properties derived from CT scans could serve as biophysical markers of PDAC, although they could not provide insight *a priori* into the natural history of the disease or underlying physical and biological mechanisms related to patient outcomes.

Here, we hypothesized that morphologic characteristics of human PDAC tumors would indicate the aggressiveness of the disease, as with other cancers (10–17). We developed a method to quantify the morphology of PDAC, classifying patients based on this imaging-based feature and correlating that classification with pathologic and clinical findings. We investigated the biophysical mechanisms related to our observations by using a mathematical theory of macroscopic PDAC tumor growth (18) that considered the stroma as a determinant of cancer cell proliferation and migration rates.

## METHODS

### Patients

All studies were conducted in accordance with U.S. Common Rule and with Institutional Review Board approval (PA14–0646), including waiver of informed consent. We reviewed patients in Supplementary Tables S1–4. Consort flow diagrams are shown in Supplementary Fig. S1. Only patients with pancreatic protocol CT scans prior to treatment were included.

**Patients who participated in a prospective trial to measure gemcitabine pharmacokinetics—**We conducted studies using data from a group of patients who enrolled on a previously described intraoperative gemcitabine infusion clinical trial (3). Briefly, patients with untreated, resectable pancreatic cancer were eligible (NCT01276613, Supplementary Table S1).

**Patients who underwent upfront surgery—**We included patients who underwent resection of treatment-naïve, localized PDAC between 2001 and 2013 (Supplementary Table S2).

**Patients who received neoadjuvant gemcitabine-based chemoradiation—**Patients who enrolled on two Phase II trials (19) of neoadjuvant therapy for resectable PDAC are described in Supplementary Table S3.

**Patients with newly diagnosed stage IV PDAC—**We included patients who presented between 2012 and 2014 with treatment-naïve stage IV PDAC, with metastatic disease either confirmed pathologically or radiographically (Supplementary Table S4).

## CT analysis

The pancreatic protocol CT scan is a diagnostic test for pancreatic cancer, where iodine-based contrast is injected intravenously at a fixed rate (20). The test usually consists of a pre-contrast phase, an arterial phase (35–40 seconds after starting contrast infusion) and a portal-venous phase (65–70 seconds after starting contrast infusion). We describe the use of each phase of the pancreatic protocol CT for our measurements below.

**i)** Delta measurement: The pre-operative CT images (2.5 mm slice thickness) were imported into Velocity AI (Varian Medical Systems, Palo Alto, CA) for image registration of the arterial phase and portal venous phase of the pancreatic protocol CT scan for each patient. After performing deformable registration of the different phases of the scan, the interface between the PDAC tumor and the surrounding pancreas parenchyma was characterized by volumetrically contouring both the tumor and pancreas at the border, while avoiding the pancreatic duct, the surrounding fat space of the pancreas, and metal artifacts. The mean value of the Hounsfield unit (HU) distribution within each contour was compared, providing a difference in HU called “delta” (Fig. 1A, B).

**ii)** Volumetric AUC (VAUC): The details of our original analysis method were described previously (2,3). We analyzed the same registered CT scans as described for the delta measurement.

## Quantitative analysis of pancreatic cancer tissue

The histologic sections of pancreatic cancer tissue stained with H&E (test set: 12 cases, see Supplementary Table S1 for patients’ characteristics; validation set: 17 cases, part of cohort in Supplementary Table S2) were scanned using a Vectra slide scanner (PerkinElmer, Waltham, MA). We used identical exposure times for all slides. The whole slide was scanned at 4X, then 100 high power images within the tumor were scanned at 20X. All

scanned images were reviewed (Vectra Review 1.0.5, PerkinElmer, Waltham, MA). Images were excluded if they were out of focus or contained artifacts. To establish the spectral library of H&E, a representative digitized image was imported to Nuance (PerkinElmer). The spectral profiles of each of these single stains were used to unmix images that contain H&E to quantify each stain. Then, we established two different image analysis methods using inForm® (PerkinElmer).

**1)** Identification of stroma cells and lymphocytes in the tumor microenvironment:

inForm® software was used to segment the nuclei of cells in the slide and subsequently identify proportions of stroma cells and lymphocytes. The software provides pattern recognition machine learning algorithms as well as cell phenotyping algorithms, which are trained to segment subcellular compartments and identify specific types of cells, respectively. A pathologist (DC) provided annotation of 1950 cells (cancer cells: 563, stroma cells: 151, lymphocytes: 310, and normal pancreas cells [islet cells: 309, acinar cells: 382, ductal cells: 235]). We established two different cell type identification training methods. First, we used four cell type classifiers (4 types, 1: cancer cells; 2: stroma cells; 3: lymphocytes; 4: normal pancreas cells). This analysis system showed high accuracy of identification of stroma cells (97.2%) and lymphocytes (98.7%). However, the accurate identification of cancer cells and normal pancreas cells (e.g. acinar cells, ductal cells, islet cells) was limited, especially when normal pancreas cells were located around cancer cells. Cancer cells were correctly identified at 81.1%, and normal pancreas cells were identified correctly at 57.4%. For comparison, we applied three cell type classifiers (3 types, 1: cancer/normal pancreas cells, 2: stroma cells, 3: lymphocytes). Both methods (3 or 4 cell type classifiers) identified the same total number of cells on each of the slides that we analyzed (range, 22,202 to 90,976 cells/slide) while maintaining a high degree of accuracy in identifying stroma cells and lymphocytes. Therefore, we used the algorithm with three classifiers to count stroma cells and lymphocytes in each slide and used the total number of cells to calculate the proportions of stroma cells and lymphocytes in each tumor.

**2)** Measurement of cellular features:

Specific images from each slide, which contained only cancer cells, stroma cells, and/or lymphocytes, were selected by a pathologist (DL). Then, the cell phenotyping algorithm with three classifiers, as described above, was applied to identify nuclei of pancreatic cancer cells (range, 1828 to 37966 cells/slide). The nucleus axis ratio was calculated as minor axis divided by major axis.

In addition to validation by a pathologist, we performed quality control measures (hematoxylin intensity of the nucleus, nucleus area, and major/minor axes of nucleus) to ensure that the cells were being identified correctly and that the measurements of the cell features were in line with expectation. ImageJ 1.48v (NIH, USA) was used to measure the major and minor axes of cells.

### PDAC primary cell lines and cell culture

MDA-PATC50, 66, 69, 102, and 118 cell lines were derived from our pancreatic xenograft program (21–23). The Institutional Review Board and the Institutional Animal Care and Use Committee at The University of Texas MD Anderson Cancer Center approved these studies. Details of cell isolation, fingerprinting, culture, and western blotting are in Supplementary Methods.

### Exome sequencing and mutation profiling

Exome DNA was captured using the Agilent 50M capture kit and tumor/normal sample pairs were sequenced with 100 base pair paired-end reads on an Illumina HiSeq 4000 sequencer at a mean depth of 150× for normal samples and 300× for tumor samples. Reads were aligned with the Burrows-Wheeler Alignment software (BWA) to the reference human genome version hg19 (24). We processed aligned reads from these tumor/normal pairs using MuTect to call point mutations and small insertions and deletions (25).

### Mathematical Modeling

We use a multicomponent mixture modeling framework to simulate solid tumor progression (10,12,26–31). Tumor and host regions are described as a saturated medium, comprised of a mixture of viable and dead cells. Volume fractions, $\phi_V$ and $\phi_D$, describe the relative amounts of these components respectively. The governing equations consist of mass and momentum balance equations for each component. The mass balance equations are

$$\frac{\partial \phi_i}{\partial t} + \nabla \cdot \left(\mathbf{u}_i \phi_i\right) = -\nabla \cdot \mathbf{J}_i + S_i, i = V, D$$

where $\mathbf{u}_i$ is the velocity, $\mathbf{J}_i$ is a flux, and $S_i$ is a source term that accounts for proliferation and death. The source terms are:

$$S_V = \Lambda_P \sigma \phi_V,$$
$$S_D = \lambda_N H\left(\sigma_N - \sigma\right)\phi_V - \lambda_L \phi_D.$$

where $\Lambda_P$ is the mitosis rate, $\lambda_N$ is the death rate associated with cell necrosis, $H$ is the Heaviside function, $\sigma$ is the concentration of cell substrates, which models the combined effects of oxygen, glucose and growth factors, $\sigma_N$ is the concentration of substrates needed for cell viability, and $\lambda_L$ is the clearance rate of dead cells. Appealing to a generalized Fick's law (27), the flux $\mathbf{J}_i = -M\phi_i \nabla \mu$, where $\mu = f'(\phi_T) - \varepsilon^2 \nabla^2 \phi_T$, with $\phi_T = \phi_V + \phi_D$, is a chemical potential. We take $f\left(\phi_T\right) = \frac{1}{4}\phi_T^2\left(1 - \phi_T\right)^2$ to be a double well potential, which reflects the tendency of the tumor cells to adhere to one another. The parameter $\varepsilon$ models the range of cell-cell interactions and introduces a finite thickness (proportional to $\varepsilon$) of the tumor-host interface.

We assume that the mixture is tightly packed so that viable and dead cells move with the same velocity, which is taken to be a generalized Darcy's law (27):

$$\mathbf{u}_i = \mathbf{u} = -\nabla p + \Lambda_M \phi_V \nabla\sigma + F_a,$$

where $p$ is the solid pressure, $\Lambda_M$ is a chemotaxis migration coefficient, $\sigma$ is the concentration of life-sustaining cell substrates, which models the combined effects of oxygen, glucose and growth factors, and $F_a = \frac{\gamma}{\epsilon}\mu\nabla\phi_T$ is a cell-cell adhesion velocity where $\gamma$ is a measure of cell-cell adhesion (27).

Assuming that the sum of the tumor and host volume fractions is constant, an equation for the pressure can be derived by summing the equations for the volume fractions (27):

$$\nabla \cdot \mathbf{u} = \Lambda_P \sigma\phi_V - \lambda_L\phi_D.$$

Finally, the cell substrates are assumed to diffuse throughout the tissue and be supplied by an underlying vasculature:

$$0 = \nabla \cdot (D\nabla\sigma) - \lambda\phi_V + S_n,$$
$$S_n = p_H(\sigma^* - \sigma)\phi_H,$$

where we have assumed that substrates diffuse sufficiently rapidly so as to enable a quasi-steady approximation, $D$ is the diffusion coefficient, $\lambda$ is the uptake rate, $S_n$ is the nutrient source, $p_H$ is the rate of substrate delivery, $\sigma^*$ is the effective level of substrates delivered and $\phi_H$ is the host volume fraction. Details of the mathematical simulations, and parameter values are in the Supplementary Methods (10,12,26–31). Here, we only discuss the estimation of the proliferation and migration parameters responsible for the morphological stability of the tumors.

### Statistics

JMP Pro 11.2.0 (SAS, North Carolina, USA) was used to perform all statistical analyses. Mann-Whitney (Wilcoxon) test was used to compare distributions between groups. Survival curves were constructed using the Kaplan-Meier method. The Cox proportional-hazards model was used for univariate and multivariate survival analyses. Overall survival was defined from time of diagnosis to time of death or last follow up for all cohorts. Distant metastasis free survival was defined from time of diagnosis to time of first distant metastasis or last follow up for all cohorts. To build multivariate Cox proportional hazards models, we started with the potential covariates which demonstrated a p-value <0.2 in the univariate models, and backward model selection technique was used. C-index was also calculated for the multivariate models. We considered a P value less than 0.05 as significant.

## RESULTS

### Quantitative Characterization of the Tumor Interface and PDAC Morphology on CT Scans

We previously demonstrated (10,11,13,28), using a biophysical theory of tumor morphologic stability (12), that the features of the tumor at the microscopic scale were described by the

competition of mechanisms that oppose infiltrative growth (termed “relaxation mechanisms,” e.g., cell proliferation represented here by the mitosis rate $\Lambda_P$) and those that promote infiltrative growth (e.g., cell migration, quantified by the chemotaxis migration coefficient $\Lambda_M$). One prediction of this model is that the tumor interface may be used to differentiate tumors that have highly proliferative cancer cells from those that are more indolent. We tested this idea by characterizing the tumor interface of PDAC on CT scans.

We developed our method to characterize the tumor interface by using pretreatment CT images from 12 patients who underwent upfront resection of PDAC (Supplementary Table S1) (3). We quantified the “delta” measurement as the volumetric difference in the mean of the Hounsfield unit (HU) distributions for the observed PDAC tumor at the border and the surrounding pancreatic parenchyma (Fig. 1A, B).

Next, two radiologists (ET, PB) ranked the conspicuity of the PDAC interface on a 1-to-5 scale (Supplementary Fig. S2) for these 12 patients (Supplementary Table S1). We found that a cutoff for the delta measurement of 40 HU distinguished conspicuous from inconspicuous lesions (Supplementary Fig. S2). We validated this result with pre-surgical CT scans of 101 patients who underwent upfront surgery for resectable PDAC (Supplementary Table S2). We performed receiver operating characteristic (ROC) area under the curve (AUC) analysis over a range of 35 to 45 HU, giving an AUC that ranged from 0.81 to 0.95, and found that the cutoff of 40 performed best in both arterial and portal venous phases. Supplementary Fig. S3A shows the ROC curves for the different delta cut offs in the arterial phase that best distinguished conspicuity of the tumors read by both radiologists. In the portal venous phase, the delta cutoff of 40 also had the best AUC (0.88 for ET’s score and 0.83 for PB’s score). Thus, we used the cutoff of 40 to define high delta and low delta groups. There was high concordance for the delta classification in 40 patients from the cohort in Table S2 for whom pancreatic protocol CT scans were performed both outside and inside our institution (kappa=0.8, Supplementary Figs. S3E, S4).

## Delta Measurement and Stroma in Tumors

The same 12 patients who provided the CT scans for developing the delta measurement (Supplementary Table S1) (3), also provided tissue samples that were scored by pathologists (HW and DC) for the amount of stroma in the resected tumors (Fig. 1C). We found a statistically significant association between the amount of stroma and the 40 HU cutoff for the delta measurement (Fig. 1D). We validated this association in another 33 patients who underwent upfront resection (Supplementary Fig. S5).

We then used a machine-learning algorithm (Supplementary Fig. S6) to identify different cellular populations on slides that were stained with hematoxylin and eosin. For the 12 patients who underwent upfront resection (Supplementary Table S1), the quantitative pathology analysis demonstrated that high delta tumors had a lower percentage of stroma cells (26±10%) than did the low delta tumors (40±5%, Fig. 1E). The percentage of lymphocytes was also significantly different between low and high delta tumors (Fig. 1F). Immunohistochemistry staining showed high delta PDAC had a higher proportion of cells that co-expressed markers for T regulatory cells (Tregs) than low delta PDAC (Fig. 1G). We found the same associations for proportions of stroma cells and lymphocytes in a second

group of patients who underwent upfront surgery for localized PDAC (Supplementary Figs. S7 and S8, Supplementary Table S2).

## Delta Measurement and Somatic Mutations Affecting Common Pathways

We reviewed 64 patients with PDAC who underwent genomic profiling (32). Fifty-two (81%) of these patients had a high delta pancreatic tumor. In the entire group, the most common somatic mutations were in KRAS (81%), TP53 (55%), SMAD4 (8%), and PIK3CA (4%). Notably, KRAS and TP53 mutations frequently occurred together (48%), followed by KRAS and SMAD4 (11%) and KRAS and PIK3CA (4%). Patients with high delta tumors were more likely to have co-occurring somatic mutations (60%) in these common genes than patients with low delta tumors (17%, Fisher's exact test, $P$=0.01, Fig. 2A). We identified 15 patient derived xenografts (PDX) from patients who underwent upfront resection of localized PDAC (23), from which we performed whole exome sequencing and mutation profiling. Considering missense and splice site mutations, of the 9 high delta PDAC samples, 7 of them had both KRAS and TP53 mutations. Of the 6 low delta samples, only 1 of them had mutations in both KRAS and TP53. Harboring mutations in both KRAS and TP53 was associated with high delta PDAC (P=0.04), where such tumors had 13.6 times higher risk of being high delta (95% CI: 0.86 −934, Fig. 2B).

## Biological and Physical Properties of PDAC Based on Delta

We isolated and characterized 5 PDAC cell lines from patients who underwent upfront surgery (23) (Fig. 3A, B). We applied the delta measurement to the preoperative CT scans from these patients. We took pictures of the cell lines at low passage in monolayer culture (less than P10), and used a membrane axis measurement to quantify cell morphology (defined as shortest axis measurement divided by longest axis measurement). We found that cancer cell lines derived from low delta tumors had significantly higher membrane axis ratios (i.e., were rounder) than those derived from high delta tumors (more elongated) (Fig. 3C). We further observed higher expression of mesenchymal marker proteins in the cell lines derived from high delta tumors than in those from low delta tumors (Fig. 3D).

Because nuclear morphology is directly associated with cellular shape (33), we further quantified cancer cell nuclear morphology by using the machine-learning algorithm on the pathology samples represented in Fig. 1. The nuclei of the cancer cells in the high delta tumors were more elongated than the cancer cells in low delta tumors, whose nuclei were rounder (Fig. 3E). This was also validated in another group of patients who underwent upfront surgery (Supplementary Fig. S7C).

We previously found that higher volumetric measurements of enhancement derived from CT scans (volumetric area under the enhancement curve, VAUC) were associated with longer survival outcomes (3). Here, analysis of 101 patients who underwent upfront resection for localized PDAC (Supplementary Table S2) and 106 patients who underwent neoadjuvant chemoradiation (Supplementary Table S3) demonstrated that patients with low delta tumors had significantly higher VAUC (0.61±0.21 and 0.65±0.22, respectively) than did patients with high delta tumors (0.40±0.20 and 0.37±0.15, respectively, $P$<0.0001 for both groups; Fig. 3F).

We next measured tumors from the patients who underwent neoadjuvant chemoradiation (Supplementary Table S3). Analysis of the distributions of the tumor axis ratios demonstrated that the high delta tumors were more likely to be round, whereas the low delta tumors were less likely to be round (Fig. 3G).

## Prevalence of High-Delta Tumors in Newly Diagnosed Metastatic PDACs

We analyzed 84 consecutive patients who presented with DM at diagnosis and received upfront chemotherapy (Supplementary Table S4). Notably, 65 (77%) of those 84 patients had a high delta in the primary pancreatic tumor (Fig. 4A, left). Survival results indicated prolonged overall survival (OS) for patients with low delta tumors (Supplementary Fig. S9A and Supplementary Table S5).

## Imaging-Based Classification, Natural Disease History, and Patient Outcomes

We extended this imaging-based classification to the CT scans of 101 patients with early-stage, resectable PDAC (Supplementary Table S2). In contrast to the patients with stage IV disease, a much higher percentage of patients in this early-stage PDAC group had low delta tumors (54%, Fig. 4A, right). Moreover, patients with high delta tumors had worse distant metastasis-free survival (DMFS) at 2 and 5 years (46% and 42%, respectively) than did patients with low delta tumors (66 and 44%, respectively, log-rank p=0.07, Fig. 4B, left). The earlier time to DM translated into poorer OS rates at 2 and 5 years for patients with high delta tumors (44% and 8%, respectively) than for patients with low delta tumors (61% and 31%, log rank $P$=0.0013, Fig. 4C, left).

The imaging delta classification was independently significantly associated with OS in multiple regression analysis, and in comparison to CA19–9, the delta classification improved the model's predictive power (c-index: 0.679 in model B vs. 0.667 in model C) (Supplementary Table S6). Exploratory analysis confined to patients with T3 disease, stratified by nodal disease, revealed a significant improvement in the c-index when the delta classification was included in the multivariate model (Supplementary Table S7). Similar analysis for CA19–9 revealed a lower c-index in the N0 group compared to the multivariate model using the delta classification (Supplementary Table S7). Sensitivity analyses of the delta measurement demonstrated significant differences in the outcomes of the patients with delta measurements in the range between 35 and 45 HU (Supplementary Fig. S10). The visual classification (i.e., scoring by radiologists; Supplementary Fig. S2) was also prognostic (Supplementary Fig. S11).

We performed a retrospective-prospective validation of the results in Fig. 4B (left) and 4C (left). The same correlations for actuarial outcomes were seen in a second dataset of 106 patients with resectable pancreatic cancer who received neoadjuvant gemcitabine-based chemoradiation (19). The delta classification was highly associated with DMFS and OS (Fig. 4B and 4C, right). Further, after neoadjuvant therapy patients with high delta tumors (20/58) were more likely than those with low delta tumors (8/48) to have progressive disease by Response Evaluation Criteria in Solid Tumors (RECIST) v1.1 (P=0.035), primarily due to distant progression. There was no difference in local progression between those with high delta tumors (8/58), compared to low delta (4/48, P=0.35). The delta classification was

independently highly associated with OS in multivariate analysis (Supplementary Table S8 and S9) and again effectuated improved predictive power when compared with CA19–9.

Because we previously found VAUC to correlate with patient outcomes and identified a cutoff of 0.6 as a way to stratify patients in terms of outcome, we explored a combined classification based on the delta score and VAUC. This combined classification seemed to subdivide patients further into different prognostic groups (Supplementary Fig. S12).

## Factors Affecting Cancer Cell Proliferation and Migration and Macroscopic Morphologic Characteristics

Motivated by recent studies suggesting that the stroma acts to restrict the metastatic spread of PDAC (7,8), we hypothesized that our mathematical theory of tumor growth could be scaled up from the microscopic level to the macroscopic tissue level by considering the stroma as a global relaxation mechanism that strongly influenced gross tumor morphology (described in Methods).

We introduce a key, dimensionless model parameter ($\Lambda$ = mitosis rate $\Lambda_P$ / chemotaxis migration coefficient $\Lambda_M$) that describes the stability of the tumor interface and represents a *ratio* of biological factors that influence proliferation and migration. We performed parametric analyses of this key model parameter to ascertain its effect on gross morphology of the tumor (Fig. 5). When the proliferation rate is slower than the migration rate (i.e., a low $\Lambda < 1$), then the model predicts that the cancer cell clusters will intermingle with the stroma, resulting in an indistinct interface for the tumor (Fig. 5A, right inset; $\Lambda$=0.2) and generating what have been described as “low mode” interface instabilities (12). Conversely, when the proliferation rate is higher than the migration rate (i.e., a high $\Lambda$ greater than the *critical value* of unity), the model predicts that the tumor cells will grow with a distinct interface, as proliferation overcomes any attempts of isolated migrating cells to separate from and leave the main tumor bulk (Fig. 5B, right inset; $\Lambda$=1.5). Representative movies of these simulations are provided in Supplementary Materials. Representative movies of these simulations are provided in Supplementary Materials (supp_info_3.avi represents low delta PDAC with lambda=0.2; supp_info_4.avi represents high delta PDAC with lambda=1.5). These simulations show direct analogy to the macroscopic features of PDAC tumors on patient CT scans (Fig. 5C and 5D).

## Growth Model Parameters and Tumor Biology Measurements

Our measurements of the pathologic specimens produce surrogates for the determinants of the stability parameter ($\Lambda$) from our model of tumor growth. To illustrate, we used the average stromal content in high delta (25±10% and 30±18%, Fig. 1D and Supplementary Fig. S5) and low-delta tumors (46±17% and 59±17%, Fig. 1D and Supplementary Fig. S5) and calculated a low-delta to high-delta stromal ratio of ~2. This ratio in stromal content would be inversely correlated with cell proliferation rates according to the model assumptions, which provides an estimate for the ratio of proliferation rates $\Lambda_P$ between high and low delta tumors. Similarly, the ratio of membrane axis ratios of cancer cells derived from low and high delta tumors is ~ 3, indicating that cancer cells from high delta tumors are

more elongated and have a mesenchymal-like phenotype (Fig. 3A-E). This number thus provides a surrogate for the ratio in migration rates $\Lambda_M$ between high- and low-delta tumors.

Therefore, the estimated ratio of stability parameters (i.e., $\Lambda_{\text{high-delta}}/\ \Lambda_{\text{low-delta}}$) is approximately 2/3, which suggests that these parameters have similar values across the two phenotypes. Accordingly, the range of the stability parameter used in the computer simulations was narrowly centered around the critical value of unity (Fig. 5 used $\Lambda = 1.5$ and $\Lambda = 0.2$). Notably, the computer simulations correctly predict the observed, different phenotypes around the critical value of unity.

## DISCUSSION

The current clinical practice for PDAC largely involves a one-size-fits-all approach. Although genetic subtypes have been identified (34,35), clinicians continue to lack reproducible, biologically meaningful, and clinically relevant biomarkers to stratify patients into prognostic groups at initial diagnosis. We have focused on the pancreatic protocol CT scan, which is a ubiquitous, standard-of-care test, to identify such a biomarker. We developed a classification of PDAC based on the conspicuity of the tumors on CT. This resulted in pathological, genetic, cellular, and clinical correlations that consistently indicate that high delta tumors are more aggressive than low delta tumors. Furthermore, our data support a mathematical theory that describes tumor morphological patterns as a balance between tumor cell proliferation and migration, providing mechanistic insight into the observed phenomena.

The advantages of this imaging-based classification of PDAC are that it can be done at the point of care before treatment, and applies to both localized and metastatic PDAC. Molecular classifications of PDAC can be challenging because they require direct pathologic sampling of the tumor (34,35). Our approach complements molecular characterizations by providing a noninvasive metric of tumor behavior. We anticipate that our imaging-defined high delta group (median survival time 13 months in resected PDAC) largely comprises the “squamous” subtype of PDAC (median survival time 13.3 months) (36), whereas the low delta group (median survival time 24 months) is a mix of molecular subtypes with better prognosis (median survival times 23.7−30 months). Our results support a molecular basis of the imaging-defined subtypes, as high delta tumors were more likely than low delta tumors to harbor multiple poor prognosis mutations in combination with KRAS, such as p53, SMAD4, and PIK3CA (Fig. 2).

Notably, mutant KRAS (37), p53 (38,39), SMAD4 (40), and PIK3CA (41,42) have been linked to immunosuppressive states through immunomodulation and recruitment of T regulatory cells. Here, we found that high delta tumors had a lower degree of stromal cell infiltrate than did low delta tumors (Fig. 1). Our findings also showed differences in the proportions of lymphocytes in high and low delta tumors. Notably, our data indicated that high delta tumors have higher proportions of Tregs in the microenvironment compared to low delta tumors. Tregs suppress immune activity and have been associated with poor outcomes in multiple cancer types, including PDAC (43). This finding agrees with our observation that patients with high delta tumors have poorer outcomes and may lead to

rational methods to stratify and select patients for stromal-modifying therapies and immunotherapy. Further, the findings in this work support the idea that the multiscale properties of cancer are intimately related to the underlying biology, which is central to the concept of oncophysics (4,44).

In addition to differing immunologic and stromal properties, we noted variability in the enhancement properties of these tumors based on the imaging. This work builds directly on our previous imaging studies of PDAC (2,3). While this study supports that low delta PDAC has a better prognosis than high delta PDAC, our previous work on radiographic changes has shown heterogeneity in responses with regard to baseline conspicuity on CT (45). A classification approach of the VAUC and delta measurements at baseline, combined with the tumor's radiographic response to therapy may further stratify patients (Supplementary Fig. S12). The heterogeneity of responses indicates differing sensitivities within each delta subtype, and *in vitro* drug testing may help clarify the molecular determinants related to the observed heterogeneity (46). Since low and high delta PDAC exhibit heterogeneity in responses to neoadjuvant therapy in the primary tumor, the difference in prognosis in these groups is likely due to differences in development of distant metastasis. Indeed, our genetic, cellular, and pathological data indicate that high delta tumors have more aggressive biology leading to a higher propensity for distant metastasis, compared to low delta PDAC.

We acknowledge that this study represents a mixture of retrospective and prospective datasets, which were not specifically designed to investigate the imaging characteristics of PDAC. Furthermore, the method of CT acquisition evolved during the study period. However, the key aspect that enables reproducible measurements of the delta is our approach to push the contrast bolus during the pancreatic protocol CT scan (Methods). This has not significantly changed during the study period, and all the scans were reviewed with our radiologists to ensure a uniform quality of scans. A future direction for this work is prospective validation of our findings in a phase II study for borderline resectable PDAC (NCT01560949), SWOG S1505 (NCT02562716), and Alliance A021501 (NCT02839343). These trials may provide further evidence that the delta classification may help predict benefit from neoadjuvant therapy.

In summary, we identified a physical feature on pre-therapy, standard-of-care CT images—the presence or absence of a distinct border between PDAC tumors and the surrounding parenchyma—that associates with cellular, pathological, biological, physical, and clinical characteristics. Each of these correlations indicates that patients with high delta tumors generally have more aggressive disease and poorer outcomes than do patients with low delta tumors (Table). These results can be used in basic and translational studies to identify how cancer/host interactions may be regulated and manipulated to alter the natural course of disease. Further, our imaging-defined subtypes can be incorporated into ongoing and future clinical trials—as well as reviews of past "failed" therapies—to identify methods to personalize and improve the care of patients with this lethal disease.

## Supplementary Material

Refer to Web version on PubMed Central for supplementary material.

## Acknowledgments

We thank Chris Wogan for her thoughtful editing of the manuscript. We also thank Mark Hurd, Amalia Gonzalez, Alexander Ondari, Christopher Bristow, and Stephanie Kerps for their research support.

Financial support:

We gratefully acknowledge partial support from the Andrew Sabin Family Fellowship, Center for Radiation Oncology Research, the Sheikh Ahmed Center for Pancreatic Cancer Research, institutional funds from The University of Texas MD Anderson Cancer Center, equipment support by GE Healthcare and the Center of Advanced Biomedical Imaging, Philips Healthcare, Project Purple, and Cancer Center Support (Core) Grant CA016672 from the National Cancer Institute to MD Anderson. Dr. Eugene Koay was also supported by NIH (U54CA210181–01, U54CA143837 and U01CA196403), the Pancreatic Cancer Action Network (14-20-25-KOAY), and the Radiological Society of North America (RSD1429). Dr. Jason Fleming was supported by the Lustgarten Foundation (989161) and Viragh Family Foundation. This work was also supported by NIH T32CA009599. Dr. Vittorio Cristini was supported by NSF DMS- 1716737, NIH 1U01CA196403, 1U01CA213759, 1R01CA226537, 1R01CA222007, the Rochelle and Max Levit Chair in the Neurosciences, and the University of Texas System STAR Award. Dr. John Lowengrub was supported by NSF DMS-1714973, NIH grants 1U54CA217378–01A1, P50GM76516 and P30CA062203. This research was partly performed in the Flow Cytometry & Cellular Imaging Facility.

## REFERENCES

1. Hidalgo M Pancreatic cancer. The New England journal of medicine 2010;362(17):1605–17 doi 10.1056/NEJMra0901557. [PubMed: 20427809]
2. Koay EJ, Baio F, Ondari A, Truty MJ, Cristini V, Thomas RM, et al. Intra-tumoral heterogeneity in gemcitabine delivery and mass transport in human pancreatic cancer. Phys Bio 2014;11:065002. [PubMed: 25427073]
3. Koay EJ, Truty MJ, Cristini V, Thomas RM, Chen R, Chatterjee D, et al. Transport properties of pancreatic cancer describe gemcitabine delivery and response. The Journal of clinical investigation 2014;124(4):1525–36 doi 10.1172/JCI73455. [PubMed: 24614108]
4. Ferrari M Frontiers in cancer nanomedicine: directing mass transport through biological barriers. Trends in biotechnology 2010;28(4):181–8 doi 10.1016/j.tibtech.2009.12.007. [PubMed: 20079548]
5. Pascal J, Bearer EL, Wang Z, Koay EJ, Curley SA, Cristini V. Mechanistic patient-specific predictive correlation of tumor drug response with microenvironment and perfusion measurements. Proceedings of the National Academy of Sciences of the United States of America 2013;110(35): 14266–71 doi 10.1073/pnas.1300619110. [PubMed: 23940372]
6. Bever KM, Sugar EA, Bigelow E, Sharma R, Laheru D, Wolfgang CL, et al. The prognostic value of stroma in pancreatic cancer in patients receiving adjuvant therapy. HPB : the official journal of the International Hepato Pancreato Biliary Association 2015;17(4):292–8 doi 10.1111/hpb.12334. [PubMed: 25250696]
7. Ozdemir BC, Pentcheva-Hoang T, Carstens JL, Zheng X, Wu CC, Simpson TR, et al. Depletion of carcinoma-associated fibroblasts and fibrosis induces immunosuppression and accelerates pancreas cancer with reduced survival. Cancer cell 2014;25(6):719–34 doi 10.1016/j.ccr.2014.04.005. [PubMed: 24856586]
8. Rhim AD, Oberstein PE, Thomas DH, Mirek ET, Palermo CF, Sastra SA, et al. Stromal elements act to restrain, rather than support, pancreatic ductal adenocarcinoma. Cancer cell 2014;25(6):735–47 doi 10.1016/j.ccr.2014.04.021. [PubMed: 24856585]
9. Hwang RF, Moore T, Arumugam T, Ramachandran V, Amos KD, Rivera A, et al. Cancer-associated stromal fibroblasts promote pancreatic tumor progression. Cancer research 2008;68(3):918–26 doi 10.1158/0008-5472.CAN-07-5714. [PubMed: 18245495]
10. Bearer EL, Lowengrub JS, Frieboes HB, Chuang YL, Jin F, Wise SM, et al. Multiparameter Computational Modeling of Tumor Invasion. Cancer research 2009;69(10):4493–501 doi 10.1158/0008-5472.can-08-3834. [PubMed: 19366801]
11. Cristini V, Frieboes HB, Gatenby R, Caserta S, Ferrari M, Sinek J. Morphologic instability and cancer invasion. Clinical cancer research : an official journal of the American Association for

Cancer Research 2005;11(19 Pt 1):6772–9 doi 10.1158/1078-0432.CCR-05-0852. [PubMed: 16203763]

12. Cristini V, Li X, Lowengrub JS, Wise SM. Nonlinear simulations of solid tumor growth using a mixture model: invasion and branching. Journal of mathematical biology 2009;58(4–5):723–63 doi 10.1007/s00285-008-0215-x. [PubMed: 18787827]
13. Cristini V, Lowengrub J, Nie Q. Nonlinear simulation of tumor growth. Journal of mathematical biology 2003;46(3):191–224 doi 10.1007/s00285-002-0174-6. [PubMed: 12728333]
14. Frieboes HB, Jin F, Chuang YL, Wise SM, Lowengrub JS, Cristini V. Three-dimensional multispecies nonlinear tumor growth-II: Tumor invasion and angiogenesis. Journal of theoretical biology 2010;264(4):1254–78 doi 10.1016/j.jtbi.2010.02.036. [PubMed: 20303982]
15. Frieboes HB, Lowengrub JS, Wise S, Zheng X, Macklin P, Bearer EL, et al. Computer simulation of glioma growth and morphology. Neuroimage 2007;37 Suppl 1:S59–70 doi 10.1016/j.neuroimage.2007.03.008. [PubMed: 17475515]
16. Edgerton ME, Chuang YL, Macklin P, Yang W, Bearer EL, Cristini V. A novel, patient-specific mathematical pathology approach for assessment of surgical volume: application to ductal carcinoma in situ of the breast. Analytical cellular pathology 2011;34(5):247–63 doi 10.3233/ACP-2011-0019.
17. Frieboes HB, Chaplain MA, Thompson AM, Bearer EL, Lowengrub JS, Cristini V. Physical oncology: a bench-to-bedside quantitative and predictive approach. Cancer research 2011;71(2):298–302 doi 10.1158/0008-5472.CAN-10-2676. [PubMed: 21224346]
18. Cristini V, Koay E, Wang Z. An Introduction to Physical Oncology: How Mechanistic Mathematical Modeling Can Improve Cancer Therapy Outcomes. New York: CRC Press; 2017.
19. Varadhachary GR, Wolff RA, Crane CH, Sun CC, Lee JE, Pisters PW, et al. Preoperative gemcitabine and cisplatin followed by gemcitabine-based chemoradiation for resectable adenocarcinoma of the pancreatic head. Journal of clinical oncology : official journal of the American Society of Clinical Oncology 2008;26(21):3487–95 doi 10.1200/JCO.2007.15.8642. [PubMed: 18640929]
20. Tamm EP, Balachandran A, Bhosale P, Szklaruk J. Update on 3D and multiplanar MDCT in the assessment of biliary and pancreatic pathology. Abdominal imaging 2009;34(1):64–74 doi 10.1007/s00261-008-9416-4. [PubMed: 18483805]
21. Kim MP, Evans DB, Wang H, Abbruzzese JL, Fleming JB, Gallick GE. Generation of orthotopic and heterotopic human pancreatic cancer xenografts in immunodeficient mice. Nat Protocols 2009;4(11):1670–80. [PubMed: 19876027]
22. Kang Y, Zhang R, Suzuki R, Li S-q, Roife D, Truty MJ, et al. Two-dimensional culture of human pancreatic adenocarcinoma cells results in an irreversible transition from epithelial to mesenchymal phenotype. Lab Invest 2015;95(2):207–22 doi 10.1038/labinvest.2014.143. [PubMed: 25485535]
23. Thomas RM, Truty MJ, Kim M, Kang Y, Zhang R, Chatterjee D, et al. The canary in the coal mine: the growth of patient-derived tumorgrafts in mice predicts clinical recurrence after surgical resection of pancreatic ductal adenocarcinoma. Annals of surgical oncology 2015;22(6):1884–92 doi 10.1245/s10434-014-4241-1. [PubMed: 25404477]
24. Li H, Durbin R. Fast and accurate short read alignment with Burrows-Wheeler transform. Bioinformatics 2009;25(14):1754–60 doi 10.1093/bioinformatics/btp324. [PubMed: 19451168]
25. Cibulskis K, Lawrence MS, Carter SL, Sivachenko A, Jaffe D, Sougnez C, et al. Sensitive detection of somatic point mutations in impure and heterogeneous cancer samples. Nature biotechnology 2013;31(3):213–9 doi 10.1038/nbt.2514.
26. Youssefpour H, Li X, Lander AD, Lowengrub JS. Multispecies model of cell lineages and feedback control in solid tumors. J Theor Biol 2012;304:39–59. [PubMed: 22554945]
27. Wise SM, Lowengrub JS, Frieboes HB, Cristini V. Three-dimensional multispecies nonlinear tumor growth--I Model and numerical method. Journal of theoretical biology 2008;253(3):524–43 doi 10.1016/j.jtbi.2008.03.027. [PubMed: 18485374]
28. Lowengrub JS, Frieboes HB, Jin F, Chuang YL, Li X, Macklin P, et al. Nonlinear modelling of cancer: bridging the gap between cells and tumours. Nonlinearity 2010;23(1):R1–R9. [PubMed: 20808719]

29. Frieboes HB, Jin F, Chuang YL, Wise SM, Lowengrub JS, Cristini V. Three-dimensional multispecies nonlinear tumor growth-II: Tumor invasion and angiogenesis. Journal of theoretical biology 2010;264(4):1254–78 doi 10.1016/j.jtbi.2010.02.036. [PubMed: 20303982]
30. Cristini V, Lowengrub J. Multiscale modeling of cancer. Cambridge: Cambridge University Press; 2010.
31. Wise SM, Lowengrub JS, Cristini V. An Adaptive Multigrid Algorithm for Simulating Solid Tumor Growth Using Mixture Models. Math Comput Model 2011;53(1–2):1–20 doi 10.1016/j.mcm.2010.07.007. [PubMed: 21076663]
32. Meric-Bernstam F, Brusco L, Shaw K, Horombe C, Kopetz S, Davies MA, et al. Feasibility of Large-Scale Genomic Testing to Facilitate Enrollment Onto Genomically Matched Clinical Trials. Journal of Clinical Oncology 2015 doi 10.1200/jco.2014.60.4165.
33. Khatau SB, Hale CM, Stewart-Hutchinson PJ, Patel MS, Stewart CL, Searson PC, et al. A perinuclear actin cap regulates nuclear shape. Proceedings of the National Academy of Sciences of the United States of America 2009;106(45):19017–22 doi 10.1073/pnas.0908686106. [PubMed: 19850871]
34. Collisson EA, Sadanandam A, Olson P, Gibb WJ, Truitt M, Gu S, et al. Subtypes of pancreatic ductal adenocarcinoma and their differing responses to therapy. Nature medicine 2011;17(4):500–3 doi 10.1038/nm.2344.
35. Moffitt RA, Marayati R, Flate EL, Volmar KE, Loeza SG, Hoadley KA, et al. Virtual microdissection identifies distinct tumor- and stroma-specific subtypes of pancreatic ductal adenocarcinoma. Nature genetics 2015;47(10):1168–78 doi 10.1038/ng.3398. [PubMed: 26343385]
36. Bailey P, Chang DK, Nones K, Johns AL, Patch AM, Gingras MC, et al. Genomic analyses identify molecular subtypes of pancreatic cancer. Nature 2016;531(7592):47–52 doi 10.1038/nature16965. [PubMed: 26909576]
37. Zdanov S, Mandapathil M, Abu Eid R, Adamson-Fadeyi S, Wilson W, Qian J, et al. Mutant KRAS Conversion of Conventional T Cells into Regulatory T Cells. Cancer Immunol Res 2016;4(4):354–65 doi 10.1158/2326-6066.CIR-15-0241. [PubMed: 26880715]
38. Kawashima H, Takatori H, Suzuki K, Iwata A, Yokota M, Suto A, et al. Tumor suppressor p53 inhibits systemic autoimmune diseases by inducing regulatory T cells. J Immunol 2013;191(7):3614–23 doi 10.4049/jimmunol.1300509. [PubMed: 24006461]
39. Shah CA, Allison KH, Garcia RL, Gray HJ, Goff BA, Swisher EM. Intratumoral T cells, tumor-associated macrophages, and regulatory T cells: association with p53 mutations, circulating tumor DNA and survival in women with ovarian cancer. Gynecol Oncol 2008;109(2):215–9 doi 10.1016/j.ygyno.2008.01.010. [PubMed: 18314181]
40. Hahn JN, Falck VG, Jirik FR. Smad4 deficiency in T cells leads to the Th17-associated development of premalignant gastroduodenal lesions in mice. The Journal of clinical investigation 2011;121(10):4030–42 doi 10.1172/JCI45114. [PubMed: 21881210]
41. Okkenhaug K Signaling by the phosphoinositide 3-kinase family in immune cells. Annu Rev Immunol 2013;31:675–704 doi 10.1146/annurev-immunol-032712-095946. [PubMed: 23330955]
42. Ali K, Soond DR, Pineiro R, Hagemann T, Pearce W, Lim EL, et al. Inactivation of PI(3)K p110delta breaks regulatory T-cell-mediated immune tolerance to cancer. Nature 2014;510(7505):407–11 doi 10.1038/nature13444. [PubMed: 24919154]
43. Yamamoto T, Yanagimoto H, Satoi S, Toyokawa H, Hirooka S, Yamaki S, et al. Circulating CD4+CD25+ regulatory T cells in patients with pancreatic cancer. Pancreas 2012;41(3):409–15 doi 10.1097/MPA.0b013e3182373a66. [PubMed: 22158072]
44. Michor F, Liphardt J, Ferrari M, Widom J. What does physics have to do with cancer? Nature reviews Cancer 2011;11(9):657–70 doi 10.1038/nrc3092. [PubMed: 21850037]
45. Amer AM, Zaid M, Chaudhury B, Elganainy D, Lee Y, Wilke CT, et al. Imaging-based biomarkers: Changes in the tumor interface of pancreatic ductal adenocarcinoma on computed tomography scans indicate response to cytotoxic therapy. Cancer 2018;124(8):1701–9 doi 10.1002/cncr.31251. [PubMed: 29370450]
46. Roife D, Dai B, Kang Y, Perez MVR, Pratt M, Li X, et al. Ex Vivo Testing of Patient-Derived Xenografts Mirrors the Clinical Outcome of Patients with Pancreatic Ductal Adenocarcinoma.

Clinical cancer research : an official journal of the American Association for Cancer Research 2016;22(24):6021–30 doi 10.1158/1078-0432.CCR-15-2936. [PubMed: 27259561]

## Statement of translational relevance

There are currently limited methods to stratify patients with pancreatic ductal adenocarcinoma (PDAC) into prognostic groups based on disease biology. We focused on the morphological features of the disease on computed tomography (CT) scans and correlated these features with genomic, pathological, and clinical data. We found that tumors with a distinct interface in relation to the surrounding parenchyma (called high delta tumors) had more aggressive biological features than tumors without a distinct interface (called low delta tumors). Patients with high delta tumors were more likely to develop early distant metastasis and die faster than those with low delta tumors. Mathematical modeling suggested that stromal elements strongly influenced the morphological patterns seen on CT scans. These findings indicate that a universally available diagnostic test can be used to interrogate the biology of this deadly disease, providing a means to stratify patients at diagnosis and aiding the design of future clinical trials.

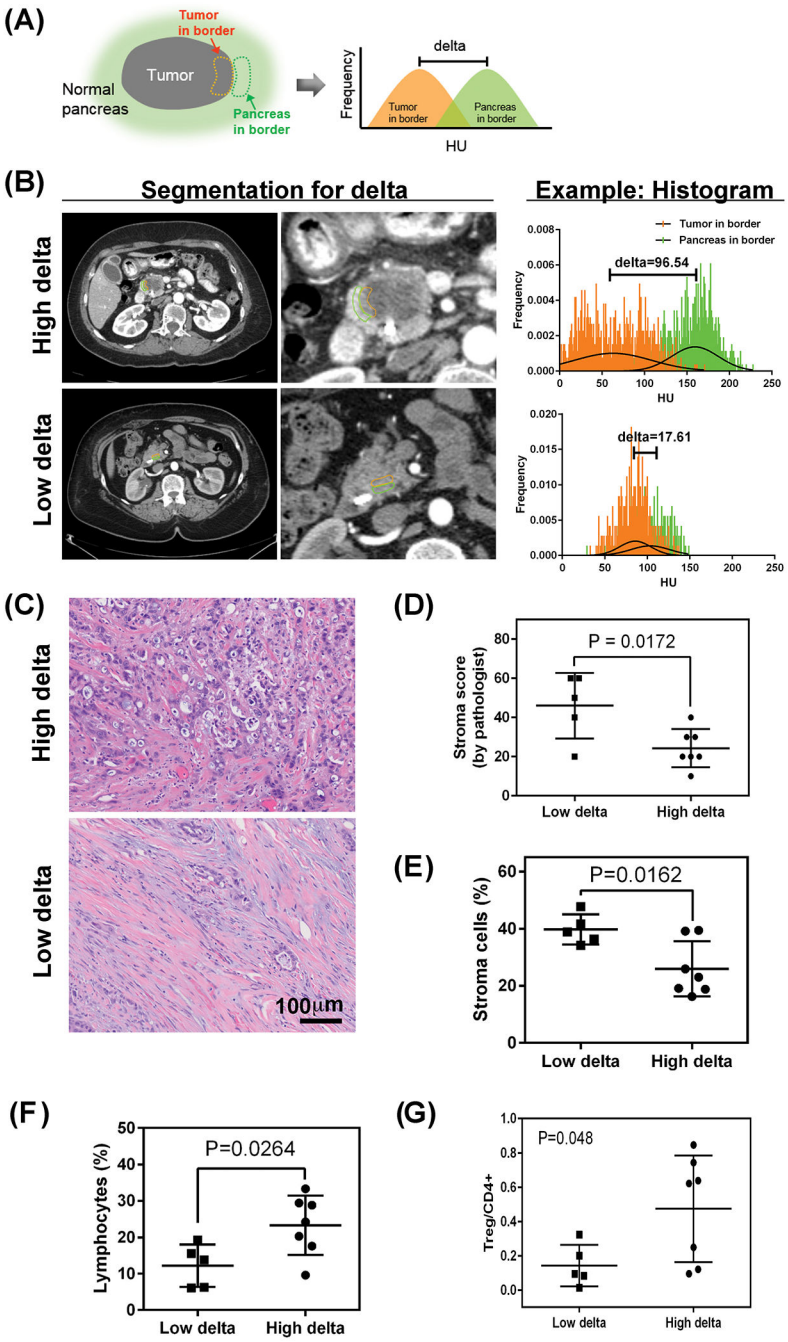


**Fig 1.**

Quantification of the interface between the pancreatic tumor and surrounding normal pancreas. (A) The “delta” method to characterize the interface of pancreatic ductal adenocarcinoma (PDAC) involves contouring the tumor at the border and the normal pancreas at the border. The Hounsfield unit (HU) distribution within each contour can be compared, providing a difference in mean HU. (B) Representative CT scans with contouring of the tumor at the border (orange) and the normal pancreas at the border (green) and the corresponding HU histogram. (C) Representative images and corresponding histology of

low- and high-delta tumors. H&E, hematoxylin and eosin. (D) Association of stroma and delta measurement in 12 patients on a trial of intraoperative gemcitabine infusion (Supplementary Table S1, also see Supplementary Fig. S5 for validation cohort). (E) The proportions of cellular subtypes from pathology specimens from 12 patients on a trial of intraoperative gemcitabine infusion (Supplementary Table S1) are shown for stroma cells (E) and lymphocytes (F). For validation, the same algorithm was applied to 17 more patients who underwent upfront resection (i.e., no neoadjuvant therapy) (see Supplementary Fig. S7, S8). (G) Association of high and low delta classification with T regulatory cell markers, normalized by CD4 positive cells.

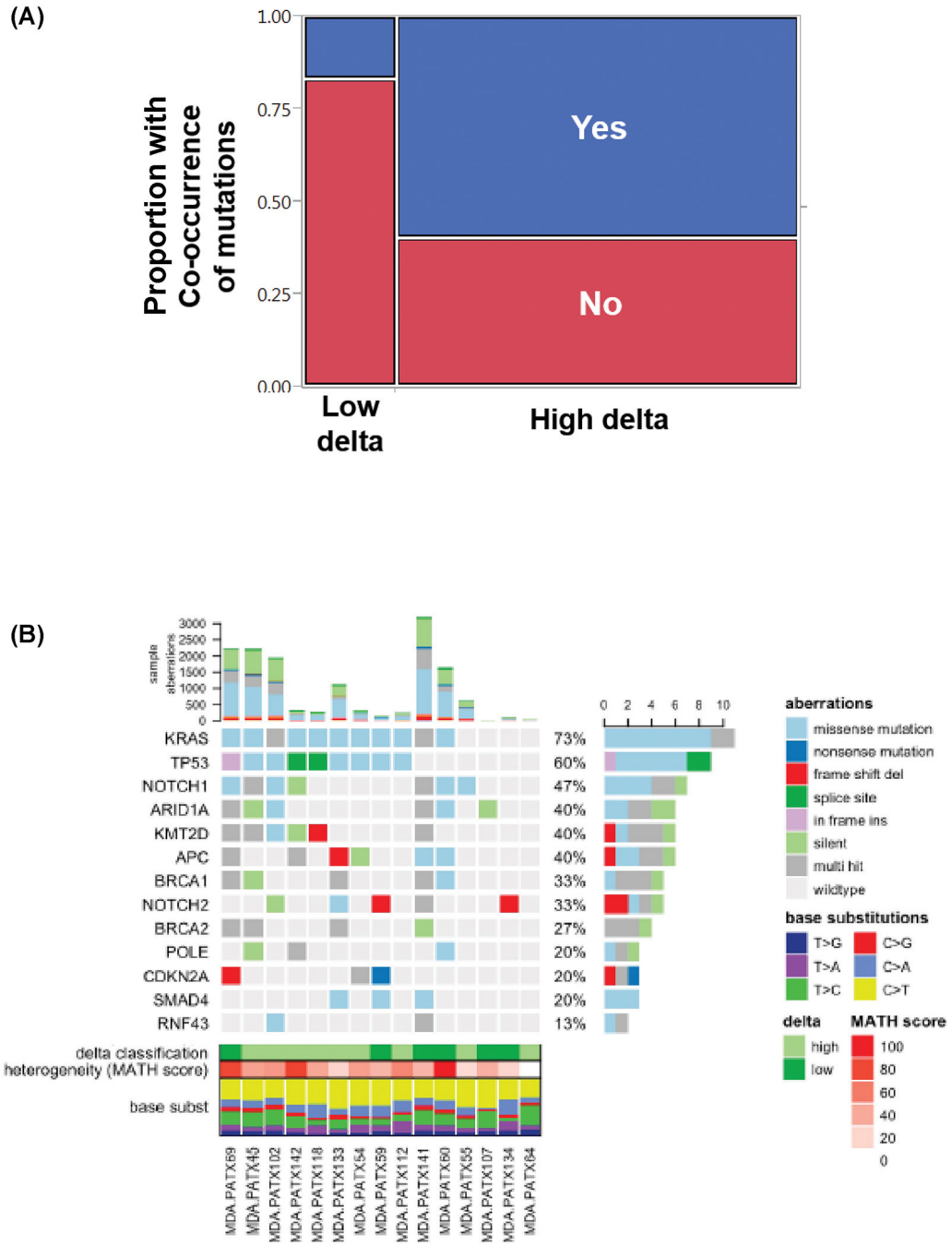


**Fig 2.**

(A) Proportions of low- and high-delta tumors in patients with co-occurring mutations, including KRAS & TP53, KRAS & PIK3CA, or KRAS & SMAD4 (Fisher's exact test, *P*=0.01). (B) Next generation sequencing data of 15 patient derived xenografts, classified according to the delta on baseline CT. High delta PDAC were more likely to harbor mutations in both KRAS and TP53 than low delta PDAC (P=0.04).

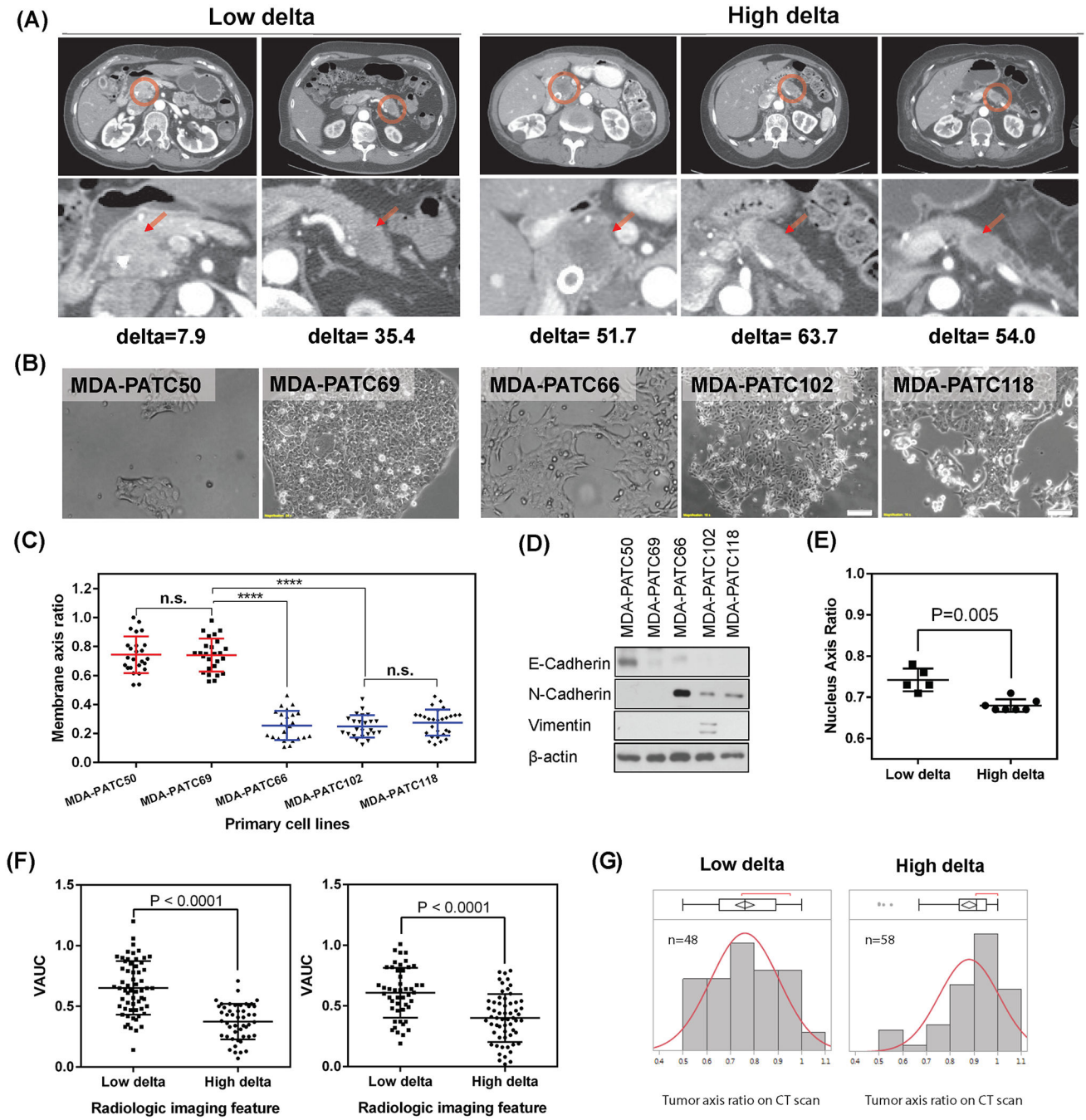


**Fig 3.**

Distinct morphologic properties of cancer cells in low and high delta tumors. (A) CT scans of 5 patients who underwent upfront surgery. (B) Cancer cell lines from the 5 patients in (A) (MDA-PATC50, −69, −66, −102, and −118). (C) The membrane axis ratio, stratified by the delta measurement (Wilcoxon test; n.s., not significant, ****$P$<0.0001). A high membrane axis ratio indicates a rounder shape. (D) Western blots of the 5 cell lines for markers of the epithelial-to-mesenchymal transition. (E) Nuclear morphology, measured from segmentation on histology. Left panel, nucleus axis ratio was measured from H&E-stained slides of 12

patients in a prospective protocol of intraoperative gemcitabine infusion during PDAC resection (Supplementary Table S1); (F) Physical properties of PDAC stratified by delta measurement, as measured by Volumetric AUC (VAUC) for patients in Supplementary Table S2 (left) and Supplementary Table S3 (right), and (G) by tumor axis ratio from CT scans with orthogonal measurements on a single axial slice at greatest tumor size for patients in Supplementary Table S3 (Wilcoxon test, $P<0.0001$).

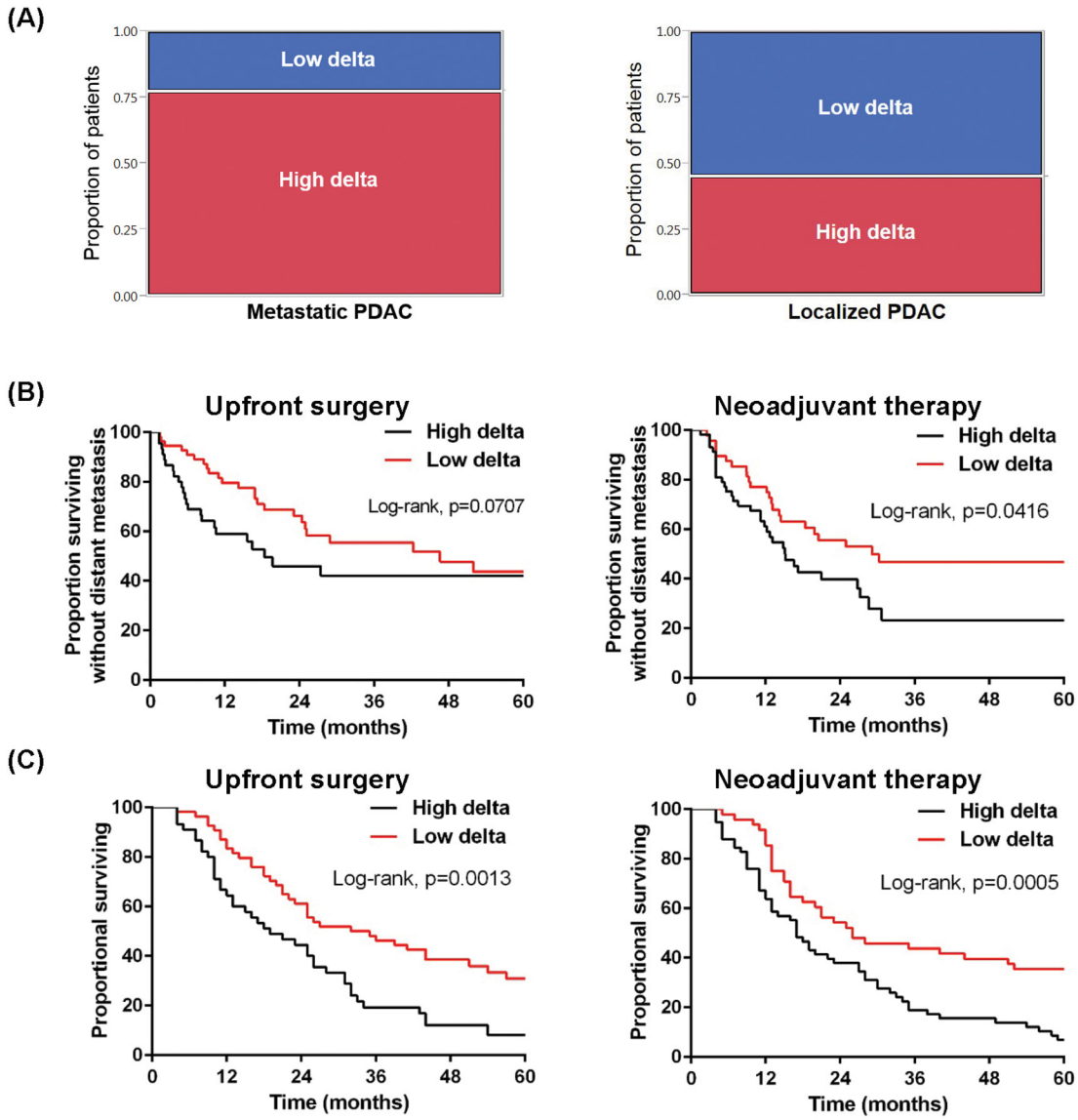


**Fig 4.**

Clinical outcomes associated with low and high delta tumors. (A) (Left) Proportions of low and high delta tumors in patients with metastatic PDAC at presentation (Fisher's exact test, *P*=0.03; patient characteristics shown in Supplementary Table S4). (Right) Proportions of low and high delta tumors in patients with early-stage, localized PDAC (patient characteristics in Supplementary Table S2). (B) (Left) Distant metastasis-free survival (DMFS) stratified by delta measurement for patients in Supplementary Table S2. (Right) DMFS stratified by delta measurement for patients in Supplementary Table S3. (C) (Left) Overall survival (OS) stratified by delta measurement for patients in Supplementary Table S2. (Right) OS stratified by delta measurement for patients in Supplementary Table S3.

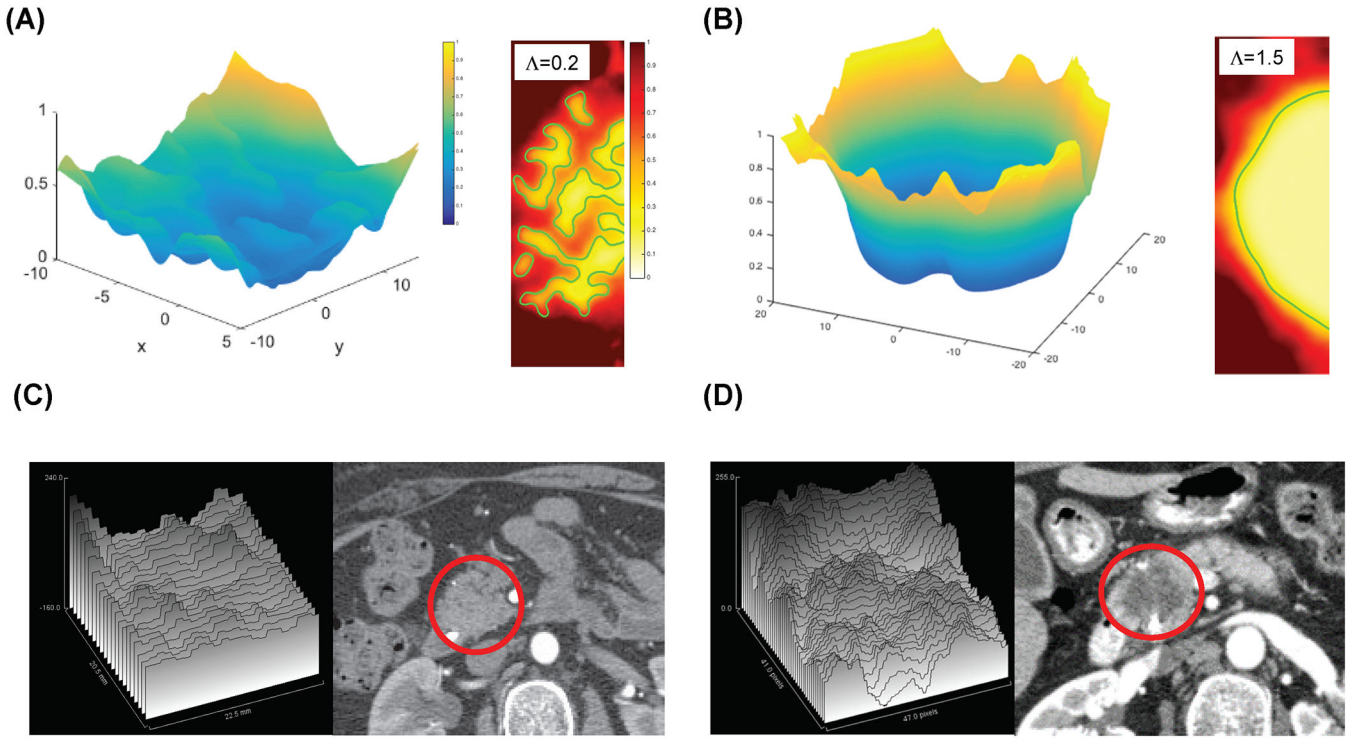


**Fig 5.**

Computer simulations of tumor interface morphology during growth. (A, left panel) and (B, left panel) represent perfusion fields predicted by the simulations, rescaled with the perfusion value in the stroma away from the tumor. The predicted change in perfusion from surrounding parenchyma to tumor is more homogeneous in tumors with relatively low cancer cell proliferation rate (Λ=0.2) (A), whereas the perfusion gradient is steeper and deeper for tumors where the cancer cell proliferation rate is high (Λ =1.5) (B). (A, right panel) and (B, right panel) represent morphology of tumors from the same two simulations. The morphology of the simulated tumors with low stability parameter $\Lambda$ shows intermingling of tumor and stroma (characterized by low-mode instabilities manifesting as large “fingers” of cell clusters (A, right inset). In contrast, for high $\Lambda$ ((B, right inset), the simulation reveals a distinct interface between tumor and stroma. Representative surface profiles (HU) generated by ImageJ of the CT images are shown in the left panels of C and D with the corresponding CT images on the right. The tumor in the CT images is circled in red.

**Table.**

Summary of differences between high- and low-delta pancreatic ductal adenocarcinomas

| | **High Delta** | **Low Delta** |
|---|---|---|
| Radiologist ranking (1-to-5 scale) | Conspicuous (4, 5) | Inconspicuous (1, 2, 3) |
| Quantitative analysis | delta ≥40 HU | delta <40 HU |
| Tumor shape | More likely to be round | Less likely to be round |
| Stroma score (by pathologist) | Less stroma | More stroma |
| Cancer cell shape | Elongated | Round |
| Multiple common mutations | More likely | Less likely |
| Patient outcome | Earlier DM, shorter OS | Later DM, longer OS |

Abbreviations: DM, distant metastasis; OS, overall survival; HU, Hounsfield Units